Contents lists available at ScienceDirect

International Journal of Heat and Mass Transfer

Local Heat Transfer Control using Liquid Dielectrophoresis at Graphene/Water Interfaces

Onur Yenigun, Murat Barisik*

Department of Mechanical Engineering, Izmir Institute of Technology, IZMIR, 35430

ARTICLE INFO

ABSTRACT

Graphene-based materials are considered for the solution of the thermal management problem of current and next generation micro/nano-electronics with high heat generation densities. However, the hydrophobic nature of few-layer graphene makes passing heat to a fluid very challenging. We introduced an active and local manipulation of heat transfer between graphene and water using an applied, non-uniform electric field. When water undergoes electric field induced orientation polarization and liquid dielectrophoresis, a substantial increase in heat transfer develops due to a decrease in interfacial thermal resistance and increase in thermal conductivity. By using two locally embedded pin and plate electrodes of different sizes, we demonstrated a two-dimensional heat transfer control between two parallel few-layer graphene slabs. We obtained local heat transfer increase up to nine times at pin electrode region with an ultra-low Kapitza resistance through the studied non-uniform electric field strength range creating highly-ordered compressed water in the experimentally measured density limits. With this technique, heat can be (i) distributed from a smaller location to a larger section and/or (ii) collected to a smaller section from a larger region. Current results are important for hot spot cooling and/or heat focusing applications.

© 2020 Elsevier Ltd. All rights reserved.

1. Introduction

Thermal management is crucial for the continuing progress in micro/nanoscale electronic, optoelectronic, and photonic devices [1]. The non-uniform heat dissipation common in most of these applications induces local hotspots, which effects the reliability of the device operation and lifetime of the components. Among the heat transfer control techniques, the two-dimensional graphene with superior thermal conductivity is considered a promising material to address the heat dissipation issues of the next generation devices [2-3] such that graphene-based smart systems with heat transfer control features have attracted considerable attention [1,4-6]. However, graphene's large interface thermal resistance creates a bottleneck for a potential heat transfer route from graphene to ambient fluid or coolant [7-10].

When two dissimilar materials come into contact, a temperature jump occurs at the interface due to the phonon mismatch known as interfacial thermal resistance (ITR). Especially with increased surface to volume ratio at micro/nano scales, ITR severely interrupts the heat transfer process. There are multiple experimental, theoretical, and computational studies regarding dependence of ITR and the resulted heat transfer onto interface properties such as

surface wetting [11], surface temperature [12], thickness of solid coating [13,14], surface atomic density [15], and liquid pressure [16]. Among these, modulating the surface wetting has been found as the most effective approach to regulate ITR. Multiple studies have been dedicated to enhancing the interface heat transfer of hydrophobic graphene by increasing the surface wettability using surface functionalization [8,9] and surface charge patterning [10], all of which provide a passive control of surface wetting. However, recent technologies require more sophisticated, active control techniques for need-based heat transfer. Surface wetting can be manipulated by an applied electric field [17,18]. In the case of an ionic liquid, a prominent net force develops on the ions, which is the conventional electrowetting-on-dielectric (EWOD) principal [19]. But, in the case of a polar dielectric liquid, a uniform electric field cannot create body forces; instead, it can manipulate molecular dipoles. We recently practiced such an idea to actively control ITR at a silicon/water interface [20]. Simply, dipolar water molecules were oriented along the applied electric field direction. This orientation polarization induced water to electro-stretch normal to surface which reduced the ITR substantially as a function of applied electric field. This systematic provides an active uniform heat transfer control through silicon and nano-confined water.

A polar dielectric liquid can also be controlled locally using a non-uniform electric field. Known as liquid dielectrophoresis (LDEP), an electromechanical force is applied on polar molecules

---

* Corresponding author.
  E-mail address: muratbarisik@iyte.edu.tr (M. Barisik).

as a Maxwell stress tensor, towards the higher electric field intensity region [21]. LDEP is frequently used as an alternative driving technique for microfluidics to execute various operations with bulk dielectric liquids, including the well-known dielectrowetting [18]. While current studies mostly employ LDEP for liquid actuation, LDEP can also be used for local manipulation of the solid/liquid coupling and resulting ITR. Such an idea will be innovative for heat transfer control at micro/nanoscales to steer heat transfer from a hotspot or toward a heat sink. To the best of our knowledge, ITR control via LDEP has never been investigated in literature.

The current work explores a graphene-based smart system applicability for thermal management purposes, where the heat transfer rate can be controlled actively and locally by an applied uniform and non-uniform electric field. We will employ Molecular Dynamics (MD) to calculate heat transfer at atomic level while corresponding electric fields will be resolved by solving the Laplace equation numerically to support MD findings. First, a one-dimensional heat conduction through water confined in a graphene channel under a uniform electric field will be examined. Later, we will examine spatial effects of non-uniform electric field and resulting two-dimensional heat transfer. We will characterize electric field induced effects in terms of change in electrohydrodynamics of water and coupling at the water/graphene interface for varying charge of electrodes.

2. Simulation Details

Non-equilibrium molecular dynamics (NEMD) simulations of water confined between few-layer graphene walls as described in Figure 1 were performed with LAMMPS (Large-scale Atomic/Molecular Massively Parallel Simulator) algorithm. First,

a uniform electric field was developed between two parallel few-layer graphene walls by defining the outmost graphene sheet at each side as electrodes and applying equally distributed charge per carbon molecule. Negative and positive charges at equal magnitudes were assigned at these opposing electrodes on each side. Applied charges per atoms were varied between 0.018 and 0.12 e per atom, which are in the range presented in the literature [7,9,22]. A computational domain with a cross-sectional area of 3.9×3.9 nm in the surface parallel directions with periodic boundary conditions was found adequate to capture corresponding physics, as the uniform electric field system develops a one-dimensional variation (Figure 1(a)). We applied a fixed non-periodic boundary condition in surface normal direction which basically acts like a vacuum as the atoms do not interact with outside of the system through this boundary. The thickness of few-layer graphene was optimized to obtain a bulk behavior in solid temperature, which was optimized to be 2 nm at each side. While the height of channel was varied as 2.8, 4, 5.7 and 7 nm, it was kept at 5.7 nm in detailed investigations. The number of water molecules was adjusted to obtain a 1 g/cm³ of bulk water density. For example, 2690 water molecules were simulated in for 5.7 nm height channel.

Second, a two-dimensional non-uniform electric field was developed between the parallel surfaces by creating a small "pin" electrode and a large "plate" electrode at the outmost graphene sheets on both sides (Figure 1(b)). Such a nano-electrode configuration can be manufactured using various techniques [23,24] to create a non-uniform electric field similar to existing dielectrophoresis applications [24,25]. These electrodes were centered in x-direction. For this investigation, we expanded the width of simulation domain as large as permitted by our computational re-
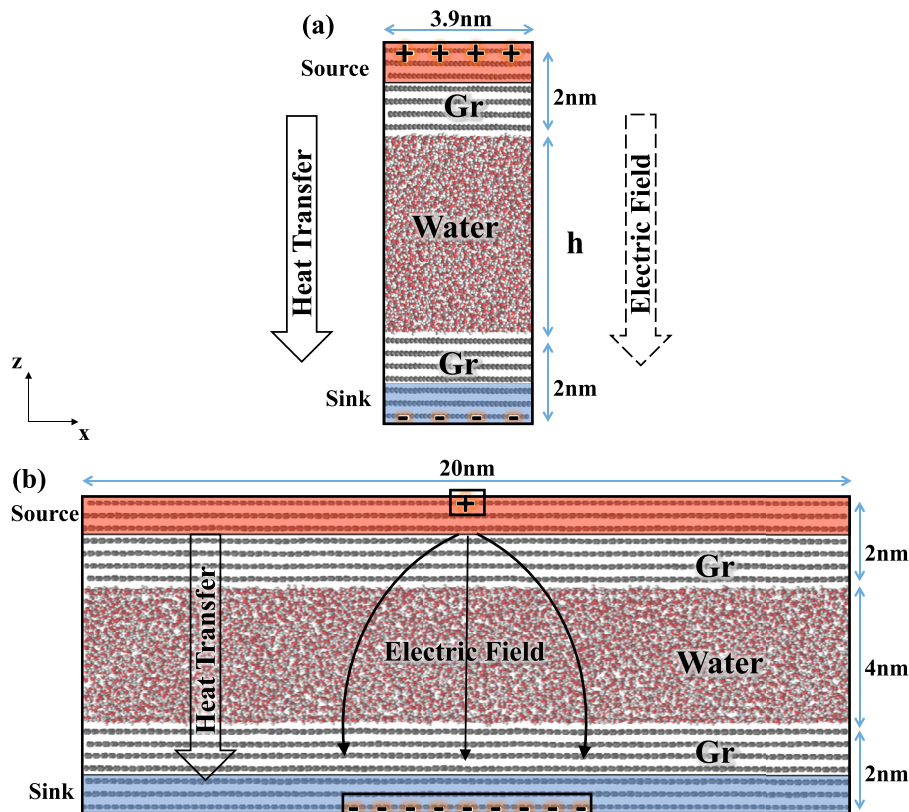

Figure 1. Simulation domain of graphene/water system for (a) uniform and (a) non-uniform electric field studies.

Table 1

Electric charges assigned on pin and plate electrodes and number of water molecules simulated at each case.

Case #	q_{plate} (e per atom)	q_{pin} (e per atom)	# of Water Mol.
1	0	0	6678
2	-0.025	0.225	6758
3	-0.05	0.45	6943
4	-0.075	0.675	7401
5	-0.1	0.9	8056
6	-0.12	1.08	8424

Table 2

Molecular interaction parameters used in the current study.

Molecule Pair	σ (Å)	ε (eV)	q (e)
O-O	3.166	0.006739	-0.8476
H-H	0	0	+0.4238
C-O	3.19	0.0040627	Varies

sources. Our objective was to develop a large enough non-uniform electric field section to capture two-dimensional variation well, while maintaining regions free from electric field effects at both ends of the simulation domain near to periodicity. Based on many trials, a cross-sectional area of 20×2.5 nm with a channel height of 4 nm were selected while the sizes of electrodes in x-direction were optimized to 0.85 nm and 7.65 nm for pin and plate electrodes, respectively. In addition to computational limitations, these electrode sizes also were optimized to maintain a physically relevant charge density values while creating a non-uniform electric filed section adequate to observe and characterize electric field effects properly. The simulation width was almost three times bigger than the size of large plate electrodes such that electric field free regions near periodic boundary conditions at both ends were properly formed. Different than a uniform case, non-uniform electric fields created a body force on the water molecules towards the high electric field intensity regions, which increased the water density as a function of the electric field. In this case, water molecules drawn closer to the near electrode regions resulted in decrease of density in the rest of the system. In order to maintain a bulk density of 1gr/cm^3 at the electric field free regions, we increased the water molecules iteratively. Table 1 lists the number of water molecules simulated at different electrode charges. Charges per atom in pin and plate electrodes were varied in a range similar with the literature [7,9,22]. Up to 8424 water molecules were modeled. Including the more than 27000 carbon atoms forming the multi-layered graphene walls, simulation domains were formed by 47000 to 52000 total number of atoms. Simulations of such magnitude required extensive computational resources and computational times.

SPC/E water model [26] composed of Lennard-Jones and Coulombic potentials is used with SHAKE algorithm which constrains the bond lengths and angles of this rigid model. It was shown that rigid water models yield very similar interfacial structures under electric field with the flexible water models [27]. The truncated Lennard-Jonnes (L-J) potentials that models the van der Waals forces is given as,

$$\Phi_{truncated}(r_{ij}) = 4\varepsilon \left(\left(\left(\frac{\sigma}{r_{ij}} \right)^{12} - \left(\frac{\sigma}{r_{ij}} \right)^{6} \right) - \left(\left(\frac{\sigma}{r_c} \right)^{12} - \left(\frac{\sigma}{r_c} \right)^{6} \right) \right),$$

(1)

where r_{ij} is the intermolecular distance, ε is the depth of the potential well, σ is the molecular diameter and r_c is the cut-off radius [28]. In addition, Coulombic potentials (Equation 2) are used to model electrostatic forces.

$$\Phi_{Coulombic}(r_{ij}) = \frac{Cq_iq_j}{4\pi\varepsilon_0 r_{ij}}$$

(2)

where ε_0 is the dielectric constant for vacuum, q_i values are the partial charges, r_{ij} is the distance between two charged pair. The Adaptive Intermolecular Reactive Empirical Bond Order (AIREBO) [29] potential is used to model the carbon atoms and their interactions. Interactions between water and graphene also calculated

by the combined Lennard-Jones and Coulombic potentials. Parameters for the interactions between similar molecules such as O–O and C–C were taken from the corresponding models. However, the parameters determining the interactions of the specific liquid/solid couples are still under investigation in literature. Frequently, interaction parameters for dissimilar molecules are calculated using simple mixing rules as a function of parameters for pairs of identical molecules. However, the interaction parameters between identical molecules are optimized for a bulk material system so that parameters calculated based on a mixing rule cannot recover the correct behavior at the given solid/liquid interface. This issue was addressed by Werder et al. through a systematic study [30]. We employed the graphene/water interaction parameters calibrated by Werder et al., and later validated by many others [9,10] (Table 2).

Atoms in the outmost layer of both sides were fixed to their original location to maintain a fixed volume system, while the remaining atoms throughout the domain were free to move. To calculate long-range Coulombic interactions of the periodic slab system, the particle-particle particle-mesh (PPPM) solver was used. The applied electrode charges were adjusted to obtain an equal amount of charge with opposite signs at pin and plate electrodes to obtain a neutral net charge in the system to satisfy algorithmic requirements of PPPM solver. Newton's equations of motion were integrated by employing the Verlet Algorithm with a time step of 0.001 ps. Simulations were started from the Maxwell-Boltzmann velocity distribution for all molecules at 323K. Initial particle distribution was evolved for 2×10^6 time-steps (2ns) under NVT condition at 323K to reach an isothermal steady state. Subsequently, one dimensional heat transfer between graphene sheets was created using the Nose Hover thermostat applied to the two outmost graphene sheets of both few-layer graphene walls. Hot and cold reservoirs were thermostated at 363K and 283K to induce heat flux through the liquid/solid interfaces. Similar temperature gradients (10-15 K/nm) can be observed in the recent technologies such as Heat Assisted Magnetic Recording (HAMR) [31,32]. The NVE ensemble was applied to the remaining carbon and water molecules. Simulations were performed for an additional 3×10^6 time-steps (3ns) to develop a steady-state heat transfer, after which simulations were performed for 25×10^6 time-steps (25ns) to obtain an adequate time averaging. Considering the large number of atoms simulated, 30ns simulation times required weeks of calculations using average of 350CPUs in high performance computing per case.

For cases with uniform electric field, one-dimensional variation of temperature was measured by dividing the computational domain into 100 rectangular bins extending through periodic y- and x-direction with a thickness of 0.097 nm in z-direction. Smaller bin thickness of 0.012 nm was also employed to resolve the fine details of the near wall water density distributions with 800 slab bins. On the other hand, simulation domain was resolved in two-dimension for the non-uniform electric field cases. For such a case, the computational domain was divided into rectangular bins extending through periodic y-direction with the size of 0.077 nm in z- and 0.818 nm in x-direction to measure temperature. Smaller bins with the size of 0.0077 nm in z- and 0.818 nm in x-direction were used to calculate water density distributions.

Irving-Kirkwood (I-K) expression is used to compute the heat flux vector for an N particle system using unity differential opera-
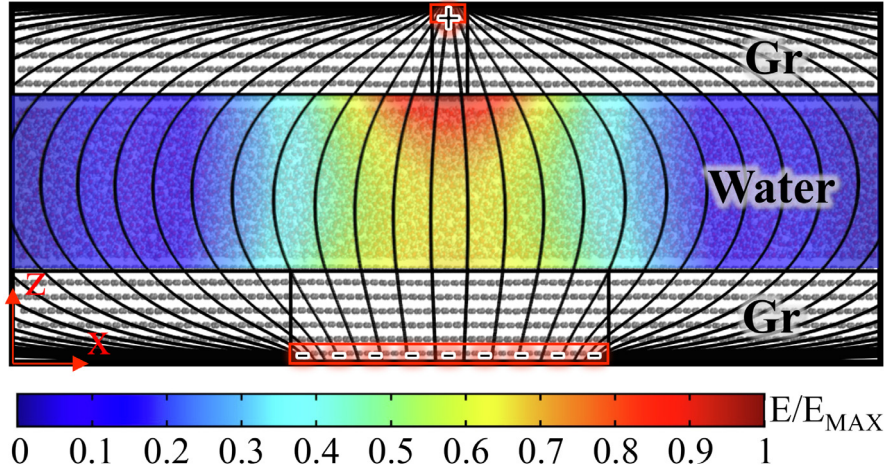
Figure 2. Simulation domain for numerical calculation by COMSOL.

tor approximation as follows [33],

$$J_k = \frac{1}{Vol}\left\langle \sum_i^N V_k^i\left(E^i + \Phi^i\right) + \sum_{i,j}^N \left(r_k^j + r_k^i\right)W^{i,j}\right\rangle, \qquad (3)$$

$$E^i = \frac{1}{2}m^i\left(\left(V_x^i\right)^2 + \left(V_y^i\right)^2 + \left(V_z^i\right)^2\right), \qquad (4)$$

$$W^{i,j} = \frac{1}{2}\left(V_x^i f_x^{i,j} + V_y^i f_y^{i,j} + V_z^i f_z^{i,j}\right), \qquad (5)$$

where, V_k^i is the peculiar velocity component of particle i in k-direction (k is the axes of the Cartesian coordinate system), E^i (equation 4) and Φ^i are the kinetic and potential energies of the particle i, $(r_k^j + r_k^i)$ is the kth component of the relative distance vector between particles i and j, $W^{i,j}$ term is given in Equation (5), where $f_l^{i,j}$ is the intermolecular force exerted on particle i by particle j in the Cartesian coordinate direction l. First term on the right-hand side of equation 3 describes the kinetic and potential energies carried by the particle i, while the second term represents the energy transfer by force interactions with the surrounding particles to particle i. By taking into account the contributions of each atom within a water molecule, an overall heat flux is calculated in the water volume using Equation (3).

For the characterization of MD results, we also performed theoretical electric field calculations. Here, our objective was to describe the variation of electric field for a given MD simulation case, in order to better explain and support the observed electro-hydrodynamics of water. We solved the Laplace equation ($\nabla^2\varphi = 0$) using finite-element scheme with COMSOL Multiphysics (www.comsol.com) to calculate the spatial non-uniform electric field ($E = -\nabla\varphi$) induced in the water domain in Cartesian coordinates as φ is the electrical potential and E is the electric field strength. A two-dimensional rectangular domain composed of graphene walls and water was designed at the same size with MD simulations, as shown in Figure 2. Pin and plate electrodes were embedded at the outermost regions of solid domains similar to MD system and electrode charges documented in Table 1 were studied while the rest of the graphene walls were appointed as zero charge boundary condition. Periodic boundary conditions were applied to the two outermost boundaries in x-direction. The mesh independent results were carefully obtained while using the model parameters of relative permittivity of water as 70.7 similar to value determined for SPC/E water earlier [34], electrical conductivity of water as 5.5×10^{-6} S/m and density of water as 0.9982 gr/cm^3 at the temperature of 293.15 K.

3. Results

3.1. Uniform Electric Field

A uniform electric field was created through the system shown in Figure 1(a) by applying uniform electrode charges on opposing electrodes at equal magnitudes but opposite signs. Resulting water density distributions at different electrode charges are given in Figure 3. We varied the charge value between 0 to 0.12 e per atom. The well-known density layering with two distinct density peaks extending couple of molecular diameter length from the surfaces develops while density reaches its thermodynamic value of 1 g/cm^3 at the center of channel away from surface effects. These density layers are formed due to the Van der Waals force field of surface and the electric field. With the increase of electrode charge, the near wall density layers are pulled towards the surface. This is the sign of the change in surface energy or surface wetting. By increasing the electrode charge, the number of molecules in near wall regions increases, which enhances the interfacial energy of the initially hydrophobic graphene surface. Furthermore, at electrode charge value of 0.053 e per atom, a solid like density distribution develops observed as density fluctuations through the whole channel as a result of electro-freezing [35,36]. This behavior can easily be seen from the simulation snapshots presented in Figure 4(a) to (f). For the electrode charge of 0.053 e and above, a hexagonal structure of (1,0,1) crystallographic ice plane [36] can be
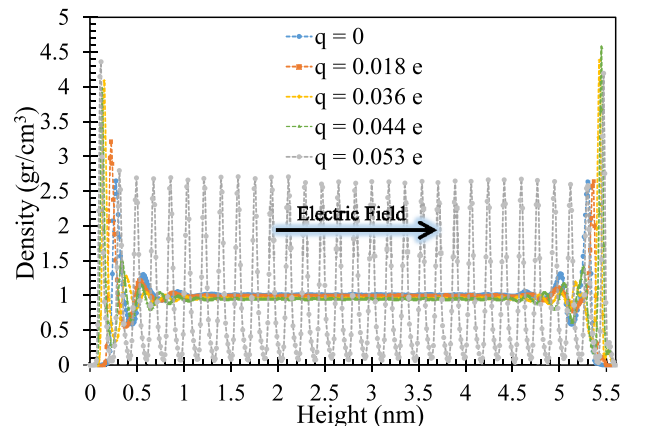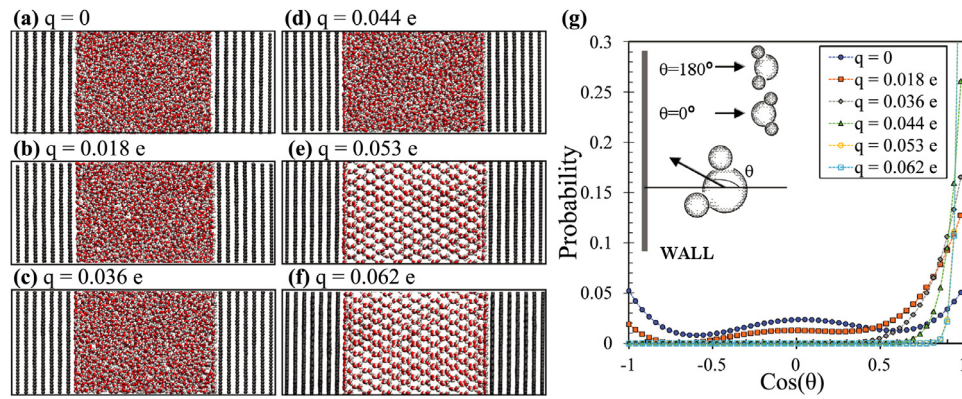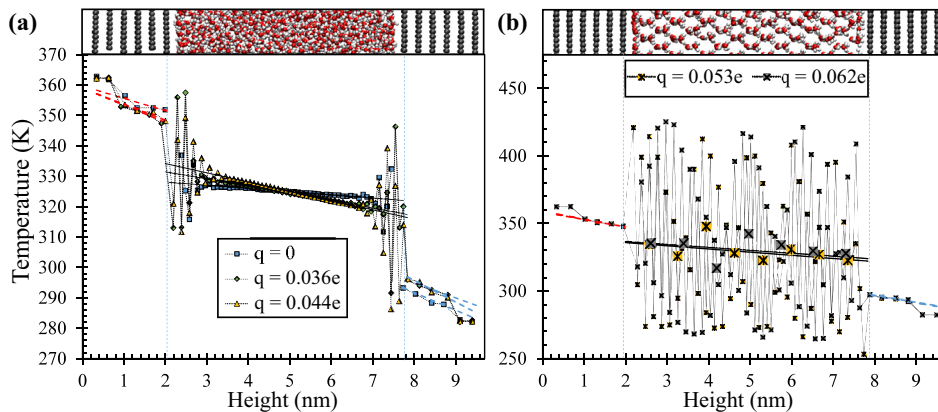

Figure 3. Density distributions at electrode charges of 0, 0.018, 0.036, 0.044 and 0.053 e per atom.

Figure 4. The snapshots of the water confined in graphene under uniform electric field with electrode charges of **(a)** 0, **(b)** 0.018, **(c)** 0.036, **(d)** 0.044, **(e)** 0.053, **(f)** 0.062 e per atom and **(g)** the corresponding probability distributions of water dipoles.

Figure 5. Temperature distributions of graphene/water system (a) before electro-freezing and (b) after electro-freezing (larger markers indicate averaged temperature profile).

observed through x-z plane. The applied electric field changes the hydrogen bond network forcing water to form a crystalline structure by electro-freezing.

As we explained in the introduction, the main influence of a uniform electric field on a polar dielectric liquid is by affecting their orientations. In order to quantify this, we measured the orientations of water molecules at varying electrode charges. We calculated the probability distributions by defining an angle (θ) between the dipole moment vector of the water molecule and the surface normal vector as shown in Figure 4(g). Simply, the cosine of the angle θ is equal to -1 when the dipole moment vector is facing towards the wall and the cosine of the angle θ is equal to 1 when pointing away from the wall. These calculations focused on the first hydration shell within the 0.5 nm distance from the wall, similar to earlier descriptions [27,37]. Variation of probabilities of cosine of each angle presented in Figure 4(g) for different electrode charges. For the zero electric field, the probability of the orientations shows an almost random and symmetrical behavior. On the other hand, when an electric field is applied, the water molecules are forced to align in electric field direction as a function of magnitude of the electric field. Hence, the probability of water molecules facing the surface increases by increasing electrode charge. Specifically, when the electro-freezing develops at 0.053 e and higher electrode charges, nearly all water dipole moment vectors align with the electric field direction.

Next, we created a one-dimensional heat conduction through these systems by assigning 363K and 283K at the opposing hot and cold reservoirs. The resulting temperature distributions are given in Figure 5 under varying electrode charges. We observed a linear variation of temperature through the water domain except the

very near wall regions, where the temperature fluctuates due to the density layering. These temperature profiles show variation by the applied electric field. Basically, the slopes of the temperature profiles increase by increasing the electrode charge. Temperature distributions of systems under electro-freezing are given separately in Figure 5(b). In these solid like systems, strong temperature fluctuations are measured with small averaging bin size. On the other hand, when a larger averaging applied, linear temperature profiles can be easily observed. It is important to note that even in a system with highly ordered water molecules, Fourier's Law of heat conduction is still applicable.

Through these heat transfer processes; sudden temperature jumps between water and graphene are observed at the interfaces due to the phonon mismatch. This is the well-known interfacial thermal resistance (ITR) which is frequently characterized by the Kapitza Length (L_K) defined as $L_K = \Delta T/(\partial T/\partial z)_{liquid}$, where, ΔT is the temperature jump at the liquid/solid interface and $\partial T/\partial z$ the temperature gradient of the liquid. We applied linear temperature fits onto temperature distribution of water and graphene in both hot and cold side. Between these linear temperature fits, we measured the temperature jumps at both hot and cold interfaces. We studied variation of ITR in terms of L_K under varying electrode charges in Figure 6(a). For no electric field case, a high L_K value of ~25nm is measured on the hydrophobic few-layer graphene surface similar to literature [38,39]. The current interfacial parameters were shown to develop 86° wetting angle [30] validating week thermal coupling. With the application of electric field, L_K shows a drastic decrease until reaching to a constant value through electro-frozen cases. This a very important outcome; prior to electro-freezing, L_K decreases up to 83% of its
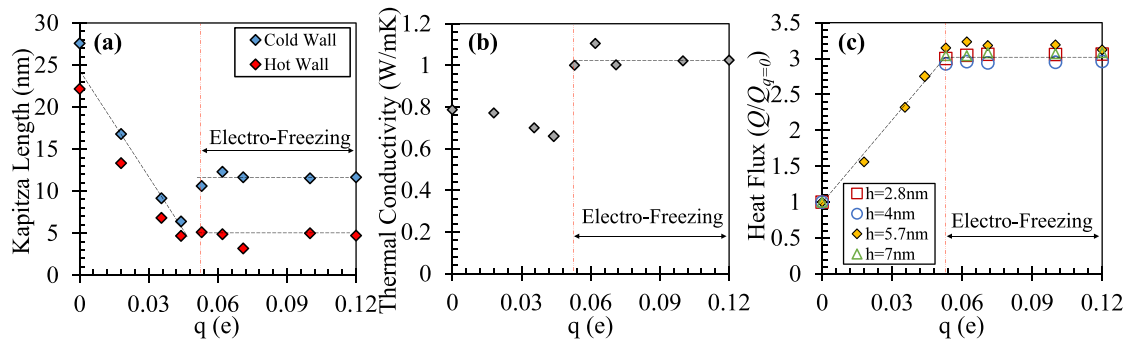
Figure 6. (a) Kapitza length and (b) Thermal conductivity of water and (c) non-dimensional heat flux as a function of electrode charge.

no electric field value. This substantial reduction of ITR is due to enhanced solid/liquid coupling at the interface or surface wetting. Earlier researchers explained the enhanced surface wetting by an applied electric field in literature [17,18]. It was also mentioned in literature that the Coulombic interactions between the charged carbon atoms and water molecules supports heat dissipation [10]. Observed behavior is also similar to enhanced interface coupling by increasing liquid pressure which also yields increasing interface layering of water [16,40]. We also observed temperature dependence of ITR. The L_K values on the hot surface are lower than the L_K values on the cold surface. This is a similar output with our previous study [12]. Two different temperature dependent variation in ITR was observed for hydrophobic and hydrophilic surfaces. While L_K increased by increasing temperature on a hydrophilic surface as a result of lessening density layering on surface by increasing temperature, an opposed behavior was observed for hydrophobic surfaces. Over a hydrophobic surface, the weak density layering develops negligible temperature dependence that L_K decreased by increasing temperature due to dominant enhanced phonon dynamics at higher temperatures. The graphene develops lower L_K values on hot surface; but by the increasing electrode charge, wetting increases that the difference between the L_K values of hot and cold surface lessens. Interestingly, L_K values of hot surface still do not exceed the values on cold surface, since the amount of electric field applied is not enough for to complete the transition of graphene from hydrophobic to hydrophilic [41]. When the system reaches to electro-freezing, the liquid domain shrinks at the crystalline form which increases the L_K values. More importantly, the thermal coupling between the solid-like crystalline water and graphene develops stronger dependence onto phonon dynamics, almost similar to the theoretically described solid-solid ITR [42]. The classical theories of phonon dynamics of solids explain enhanced phonon activities at higher temperatures well. At electro-frozen condition, crystalline water vibrates less increasing the phonon mismatch at cold surface higher than its value at liquid case.

In addition to ITR, we studied the electric field effects on thermal conduction through the water domain. The thermal conductivities of water under different electric fields were calculated from the liquid temperature gradients using Fourier's Law as $k = q/(\partial T/\partial z)_{liquid}$, where k is the thermal conductivity of water and q is the heat flux through the system. Figure 6(b) presents the k values for different electrode charges. At zero electric field, thermal conductivity is calculated as 0.8 W/mK at the average temperature of 325 K, which agrees with the literature [43,44]. This value is slightly different than the experimental measurements due to the limitations in SPC/E model as explained by earlier researchers [44,45]. Conductivity decreases some prior to electro-freezing due to the restricted molecular diffusion and hydrogen bonding activities of water molecules under electric field. After reaching the crystalline structure, conductivity shows a sudden jump and then re-

mains constant with the increased electric field. Change in water thermal conductivity is not as dominant as the change in ITR under increasing electric field.

As a result, the total heat transfer through water/graphene system varies by electric field; the heat flux substantially increases up to 3 times by an applied electric field as shown in Figure 6(c). This major enhancement is basically due to large decrease in ITR under electric field. Heat flux reaches this value right at electro-freezing after which it remains constant. We further explored this behavior at different height confinements. We modeled different channel heights of 2.8, 4, and 7 nm. For these cases, we only focused on zero electric charge case and five different electrode charge values corresponding to electro-freezing conditions. Different height systems develop different heat flux values for the same temperature difference applied between the hot and cold reservoirs. For comparison, we normalized each case by its value at no-charge. A universal behavior is observed in normalized heat flux behavior presenting negligible confinement height dependence at these scales.

3.2. Non-uniform Electric Field

Up to this point, we described a uniform manipulation and control of the of ITR and resulting heat transfer between graphene and water. From here, we will practice the local control of heat transfer by a non-uniform electric field. For this purpose, we defined a smaller pin electrode and a larger plate electrode centered at the width of graphene/water system. We extended simulated domain to obtain regions with negligible electric field near periodic boundaries at both ends. By this way, we attained a proper periodic effect on heat transfer physics to measure only influence of the given non-uniform electric field. The simulation and electrode sizes were optimized to cover an adequate resolution of non-uniformity in two-dimension allowed by our simulation capabilities. Different than the uniform case, a net electrostatic force develops on water molecules under non-uniform electric field. We should note here that similar electrostatic forces develop in the earlier uniform electric field cases as well, but forces on negative and positive poles of water molecules are equal to each other yielding zero net force; they only create a torque which eventually is the reason for the alignment of dipoles in electric field direction. For non-uniform electric field, forces developing on opposite sides of a water molecule become different as the electric field is non-homogeneous. Such a net electric field force on a dipole can be approximated as $\vec{F} = \vec{p} \cdot \vec{\nabla}\vec{E}$ as a function of the water dipole moment vector ($\vec{p}$) and the gradient of electric field in tensor form ($\vec{\nabla}\vec{E}$). While the water dipoles tend to get in line with electric field direction, a net body force is expected to develop on a water molecule in electric field gradient direction towards the higher electric intensity regions.

We started our characterizations by calculating the theoretical electric field distributions in the system at the studied electrode charges. To specify a simulation case, we used charge value of its plate electrode while the charge on corresponding pin electrode was assigned inversely proportional to electrode size at opposite sign. By this way, the total charge on the plate and pin electrodes were equal to each other to maintain a zero net charge in the system required by LAMMPS calculations. Figure 7(a)-(f) present electric field contours and lines as the solution of the Laplace equation using the finite element solver COMSOL. Electric field results at different electrode charges were normalized with the maximum electric field strength (2.05 V/nm) measured through all these cases, which is at 0.12 e plate electrode charge. At each case, highest electric field strength develops near the pin electrodes. Electric field decreases away from both electrodes towards periodic boundaries. Results show the non-uniform electric field and the resulting two-dimensional variation of electric field intensity through simulation domain. The electric field lines describe the direction of the electric field vectors in each system. The molecular snapshots of the MD simulations under the corresponding non-uniform electric fields are presented in Figure 7(g)-(l) at different electrode charges. First, we can easily observe that an LDEP force develops increasing the water population near electrode regions. By increasing the electric field, we observed the bending of graphene layers at both pin and plate electrode sides. This behavior becomes evident starting with the electrode charge of q_{plate}=0.05 e. Next, we calculated water dipole vectors in two-dimensional space. Figure 7(m)-(r) presents directions of water dipole vectors as blue arrows on top of corresponding simulation snapshots. The influence of the electric field can be observed easily as the random distribution of dipole vectors at no electric charge changes quickly by application of electrode charges. At q_{plate}=0.05 e, line-up of dipole vectors in electric field directions between the electrodes becomes obvious. This shows that the system is undergoing an electro-freezing like ordering, even the molecular picture of the system does not show a crystal structures due to the non-uniform electric field. This result is also consistent with the uniform electric field conditions as the electro-freezing started at a similar q=0.053 e. With an increase of electrode charges, more dipole moment vectors align with the electric field lines given through Figure 7(a)-(f). The solid-like ordering of water is clearer for these cases in simulation snapshots. These are not perfect crystal structures formed under uniform electric field, but mostly appear as multi grain structures compressed towards the regions with high electric field intensities. Away from electrodes, we observed mostly random dipole distributions near periodic boundaries, except the highest electrode charge of q_{plate}=0.12 e. The effect of LDEP forces can also be seen clearly from the density contours in two-dimension given in Figure 7(s)-(x). Water density of 1 gr/cm^3 is measured in most of the channel except the near interface region developing well-known density layering while the few layer graphene density is 2.267 gr/cm^3 similar to literature [46]. With an increase in electrode charges, this solid-like water layering increases and grows towards channels bulk. High local water densities are measured near interface similar to density layering observed over highly hydrophilic surfaces by earlier studies [16]. As the non-uniform electric field forces water molecules to move towards the high electric field gradient region, ice-like average density values are observed similar to literature reporting density values as high as 2.51 g/cm^3 bulk density [47-49]. The electro-freezing formation starting from near electrode regions towards the bulk liquid can be easily observed by solid like water density variation. This local density structuring is very similar with the local variation of the non-uniform electric field shown in Figure 7(a)-(f). As explained earlier, LDEP forces pull water molecules towards the near electrode regions which yields an increase in density as a function of electric field, and depletion in

the rest of the simulation domain. We compensated for this by adding further water molecules in simulation domain until the regions near periodicity reaches to bulk value of 1g/cm^3. We should also note here that water density increases near both pin and plate electrodes, but pin electrode region develops a higher density increment. While water molecules away from electrodes were unaffected, the local water density and resulting pressure were varied in two dimensions as a function of the non-uniform electric field.

Next, we developed heat transfer by assigning 363K and 283K temperatures at the outmost two layers of both graphene walls on opposite sides. Figure 8 presents the two-dimensional temperature contours of water domains under increasing electrode charges while heat transfer and electric field are at the same direction and pin electrode is located at the hot reservoir side. Due to the extremely high in-plane thermal conductivity of graphene, each graphene layer remains at an almost constant temperature in x-direction along the channel. Graphene temperature only varies in cross-plane direction normal to interface. For this case, each graphene layer was shown as a line and its constant temperature values were written on the figures. At zero-electric field (Figure 8(a)), a one-dimensional variation of water temperature normal to interface can be clearly seen. Once the electric field is applied, water temperature starts to vary in two-dimension; specifically, temperature near electrode regions increases at hot reservoir and decreases at cold reservoir side, as a function of electric field strength values. Simply, the substantial temperature jumps between graphene and water at both hot and cold sides decrease as a result of increased thermal coupling by electric field. With an increase in electrode charge, this non-uniform temperature variation between the electrodes becomes very prominent, and water and graphene surface temperatures are almost equalized at high electric strength regions. Convergence of water temperature to graphene surface temperature is stronger at pin electrode side due to higher LDEP forces. Specifically, pin electrode region has a higher thermal coupling allowing higher heat transfer through a specific local spot. Such local control of thermal coupling would be desired in the case of a hot-spot cooling or heat flow guiding.

We started to characterize the non-uniform heat transfer by calculating the local ITR in terms of Kapitza length. We defined local regions with a width equal to pin electrode size through the channel as shown in Figure 9(a). We averaged the temperature values in x-direction inside these regions and obtained a single temperature profile in z-direction for each region. Even though the current non-uniform system has two-dimensional temperature variation, these one-dimensional water temperature distributions determined in local regions were very close to linear behavior. Similar to the systematic used in earlier uniform electric field section, the temperature jumps at both hot and cold interfaces were measured between the applied linear fits of water and graphene temperature distributions. Calculated L_K values of hot and cold interfaces are given in Figure 9 (b) and (c). At zero electric field case, high L_K values of 22.5 and 27.5nm were measured showing week thermal coupling between graphene and water. These values and temperature dependence of L_K are similar to earlier results and discussions. By the application of electric field, L_K shows a drastic decrease at regions close to pin and plate electrodes. This reduction in L_K lessens away from the electrodes as both electric field strength and LDEP forces decreases. While at q_{Plate}=0.025 e case develops almost no change in L_K away from electrode regions, increasing electrode charge yields decrease of L_K near periodic regions. This change is not as dominant as the L_K reduction in between the electrodes. Hence, we can still consider that we captured local influence of non-uniform electric field with appropriate periodic conditions in the axial extent. The influence of non-uniform electric field on to the graphene/water interface are by (i)
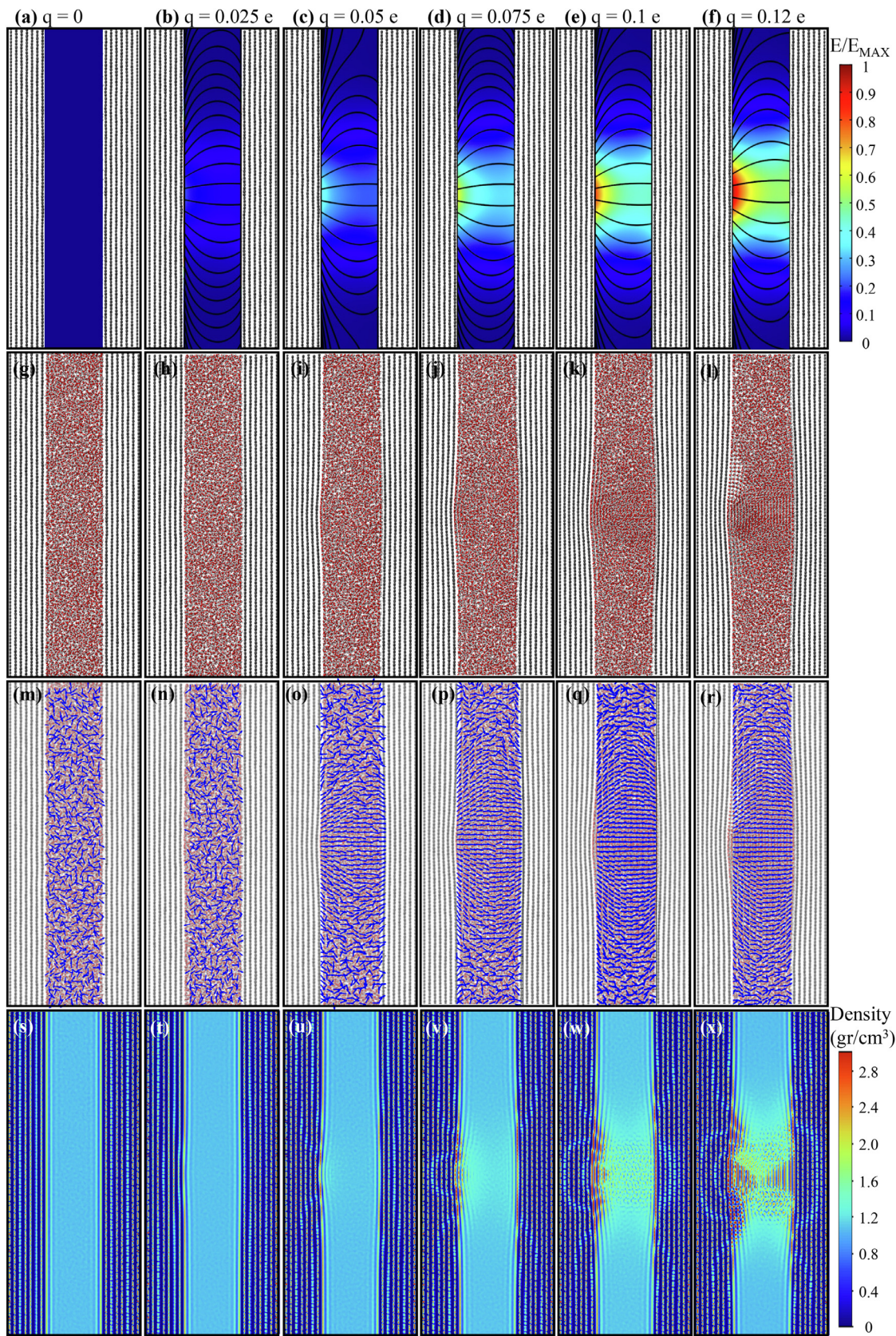
Figure 7. **(a-h)** Electric field contours, **(g-l)** molecular orientations, **(m-r)** dipole moment vectors of water molecules and **(s-x)** density contours at different electrode charges.
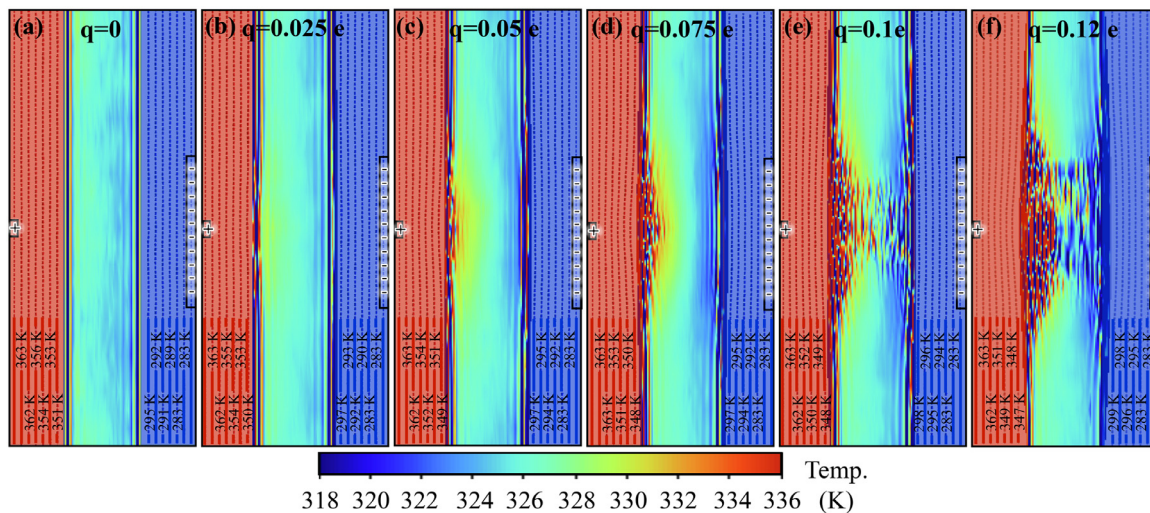
Figure 8. Temperature contours at different electrode charges of (**a**) q_{plate}=0, (**b**) 0.025 e, (**c**) 0.05 e, (**d**) 0.075 e, (**e**) 0.1 e and (**f**) 0.125 e.
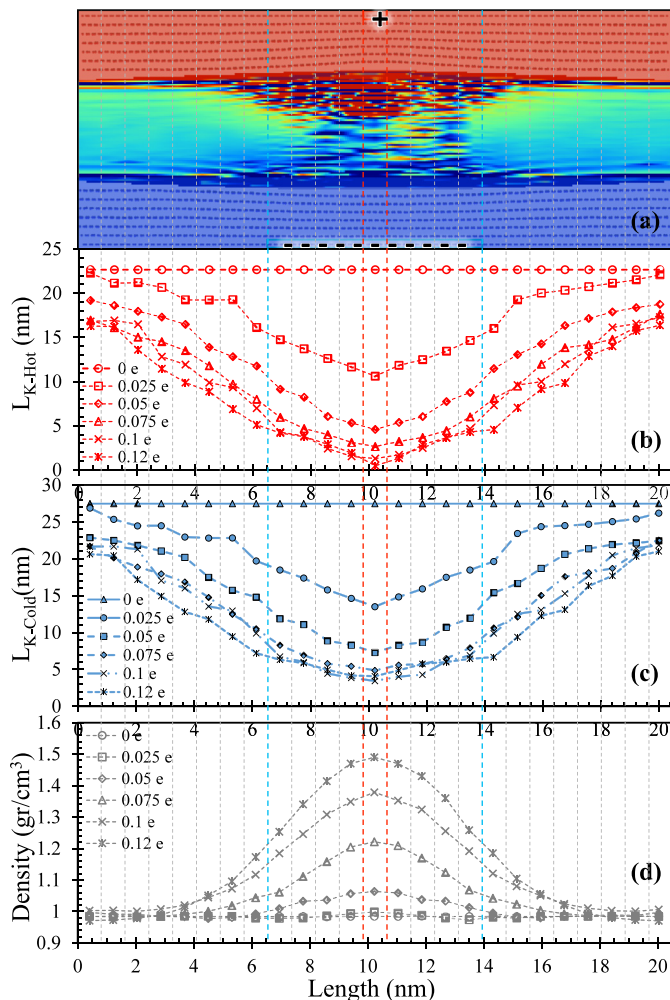

Figure 9. (**a**) Representation of the regions for local measurements. Temperature counter of q_{plate}=0.12e case was used in figure. Local variation of (**b**) L_{K-Hot}, (**c**) L_{K-Cold}, and (**d**) water density measured at each local region for different electrode charges.

enhancing the Columbic interactions, (ii) aligning the water dipoles in electric field direction yielding electro-stretching, and (iii) creating LDEP forces directed toward the higher electric field regions. These three major mechanisms increase the interface coupling as a function of the local electric field and its gradient that L_K shows strong variation as a function of the non-uniform electric field. We calculated an average water density in each of these local regions to characterize the increase of pressure due to the exerted body forces by LDEP. At low electrode charges of 0.025 and 0.05 e, L_K in both pin and plate side shows 50% and 80% decrease, but density shows a negligible change through the channel. By increasing electrode charge to 0.075 e, L_K undergoes a 90% decrease while density shows up to 20% increase in line with pin electrode region. By further increase of electrode charge yields almost negligible ultra-low L_K values (~0nm) at the pin electrode, and water density continues to increase. Decreasing L_K by increasing density and pressure was also shown in detail in our previous work [16].

Next, we focused on characterization of local L_K values measured along the pin and plate electrode regions as a function of applied charge. We averaged the local L_K values to coincide with plate electrode extent at cold reservoir side and refer it as $L_{K-Plate}$. Similarly, L_K value measured in line with pin electrode at the hot side was labeled as $_{LK-Pin}$. We compared the L_K results of non-uniform electric field with the results of earlier uniform electric field case ($L_{K-Uniform}$) in Figure 10(a). The $L_{K-Uniform}$, L_{K-Pin} and $L_{K-Plate}$ values actually present very similar behavior until the electro-freezing around q=0.05 e. In this charge range, both uniform and non-uniform cases develop up to 83% decrease in L_K values. Interestingly, $L_{K-Uniform}$ and L_{K-Pin} are almost identical while $L_{K-Plate}$ has slightly higher values. This is due to both lower LDEP in plate electrode side and reduced phonon activities at the lower temperature. We should note here that in this charge range, LDEP does not create much of a pressure build up in between the non-uniform electrodes. Hence, we can simply state that the uniform and non-uniform electric fields create very similar heat transfer enhancement in low electrode charge range. Actually, a uniform electric field can also be utilized for local heat transfer control in between two opposing finite and **equal size electrodes**. But non-uniform field can provide local heat transfer control between **different size regions**, which allows the **collection and distribution of heat to/from a smaller location from/to a larger region**. Simply, for the current configuration as pin electrode is on the hot side, the reduced L_K at a small local spot near pin electrode increases heat removal from that location, while the removed heat is trans-
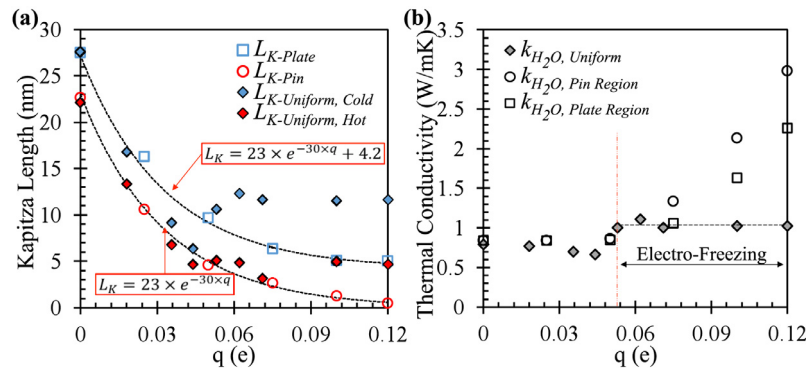
Figure 10. (a) Kapitza Length values at hot and cold interfaces under varying uniform and non-uniform electric fields. **(b)** Local water thermal conductivities in line with pin and plate electrodes compare to water thermal conductivity under uniform electric field.

ferred to a larger area on the other side of the channel through reduced L_K region near the plate electrode.

Starting with q_{Plate}=0.05 e, increase of electrode charge creates no further decrease in ITR under uniform electric field that the lowest ITR remains as L_K=5 nm on the hot side. Instead, the non-uniform electric field continues to decrease the ITR. The advantage of LDEP particularly reveals itself in this charge range as it allows to obtain ultra-low ITR values. Simply, L_{K-Pin} undergoes a 99% reduction at q_{Plate}=0.1 e and becomes almost zero at q_{Plate}=0.125 e. Another main advantage of non-uniform field also appears after electro-freezing as it continues to create low L_K for the cold surface side different than the uniform case. The cold surface under uniform electric field undergoes strong temperature dependence starting with electro-freezing at q_{Plate}=0.05 e and develop an L_K increase to 12 nm compare to its prior to electro-freezing value of 6 nm. Instead, the non-uniform case attains very low L_K value by the help of LDEP body forces. Basically, LDEP offsets the lower phonon activities so that cold surface develops only slightly higher L_K than hot side under non-uniform electric field. In order to characterize the variation of L_{K-Pin} and $L_{K-Plate}$, we applied mathematical fits as a function of the electrode charge. An exponential decrease of L_{K-Pin} and $L_{K-Plate}$ are observed while the difference between them remain almost constant through different electrode charges.

As we performed long averaging times, fluctuations in temperature due to dynamic nature of phonon-interface interactions were maintained at low levels. We analyzed the statistical variation in our results to determine the error margins. Using the total simulation time of 25ns, different time averages obtained at every 2ns, 5ns, 10ns and 25ns. These 20 different data sets yielded 20 different L_K values, based on which the standard deviations in L_K measurements were obtained. Specifically, Kapitza values of different charge values at the pin electrode side with error margins were $L_{K-Pin-q=0e}$=22.6±0.97nm, $L_{K-Pin-q=0.025e}$=10.65±0.9nm, $L_{K-Pin-q=0.05e}$=4.59±0.44nm, $L_{K-Pin-q=0.075e}$=2.66±0.18nm, $L_{K-Pin-q=0.1e}$=1.29±0.25nm and $L_{K-Pin-q=0.12e}$=0.4±0.32nm. By increasing electrode charge, fluctuations and error values were found decreasing. Even though low L_K results of high electrode charges becomes comparable to statistical fluctuations, errors are at negligible range. As the local results at small pin electrode side were measured from small averaging bins containing limited number of molecules, fluctuations and errors of L_K values from larger plate side were smaller than pin electrode errors and negligible.

We continued by characterizing the thermal conductivity of water under non-uniform electric field. Based on the local water density values measured in each region given in Figure 9(d), we calculated water thermal conductivities based on literature [43,49,50]. Specifically, local water thermal conductivities in each region taken from thermodynamic tables provided by Ref. [50] except the high

near electrode densities (ρ_{water}>1.2kg/m^3) developing at high electrode charges of $q_{Plate} \geq 0.075$ e. For these densities corresponding to solid-like compressed water, we used the data provided by Ref [43] and Ref [49] for 300K. Water thermal conductivities for pin and plate electrode regions at different electrode charges are given in Figure 10(b) compare to results of uniform electric field cases. Prior to electro-freezing, a slight decrease of thermal conductivity develops, but it is less than uniform electric field case as the molecular diffusion of water is restricted less under non-uniform electric field. After which, LDEP forces create density increase so the thermal conductivity increases. Electro-freezing under uniform electric field creates a single crystalline structure which enhances thermal conductivity substantially. Differently, non-uniform electric field does not yield a single crystalline structure such that thermal conductivity does not show any significant increase around q_{Plate}=0.05 e. Instead, thermal conductivity shows a gradual increase by increasing electrode charges due to increasing density and solid-like molecules ordering of water under non-uniform electric field. This eventually yields higher thermal conductivities than uniform case for q_{Plate}=≥0.75 e cases. Water conductivity at pin electrode side is higher than plate side when the LDEP forces becomes prominent.

At this point, we also considered the possible influence of the direction of heat transfer compared to the direction of electric field and the location of pin electrode. Up to here, we studied cases where both heat transfer and electric field are in the same direction, and pin electrode is on hot reservoir side. However, different configurations are possible. In literature, the directional dependence of the heat transfer through a non-homogeneous domain is described as "thermal rectification" which has been studied for various systems including graphene. For instance, it was presented that in-plane heat transfer of a graphene layer consisting non-uniform/asymmetric structural defects [51] or solid stiffness [52] shows strong directional dependence. Simply, the asymmetricity of a system allows an easier heat transfer in one direction than the heat transfer in the same axis but in the opposite way. In our case, the non-uniform electric field creates non-homogenous interface coupling and water structuring that we wanted to test our system for possible heat transfer rectification. First of all, we observed that direction of electric field has no effect on heat transfer. The water dipole orientation changes according to electric field direction, but very similar water structuring and ITR develop through the system independent from direction of electric field. For such a case, we tested our system by changing the heat transfer direction where pin electrode is on cold reservoir side. We applied q_{Plate}=0.1 e since it yields a distinct non-uniformity as the electric field dominated region in between the pin and plate electrodes develops an almost "triangular shape" non-uniform electric field
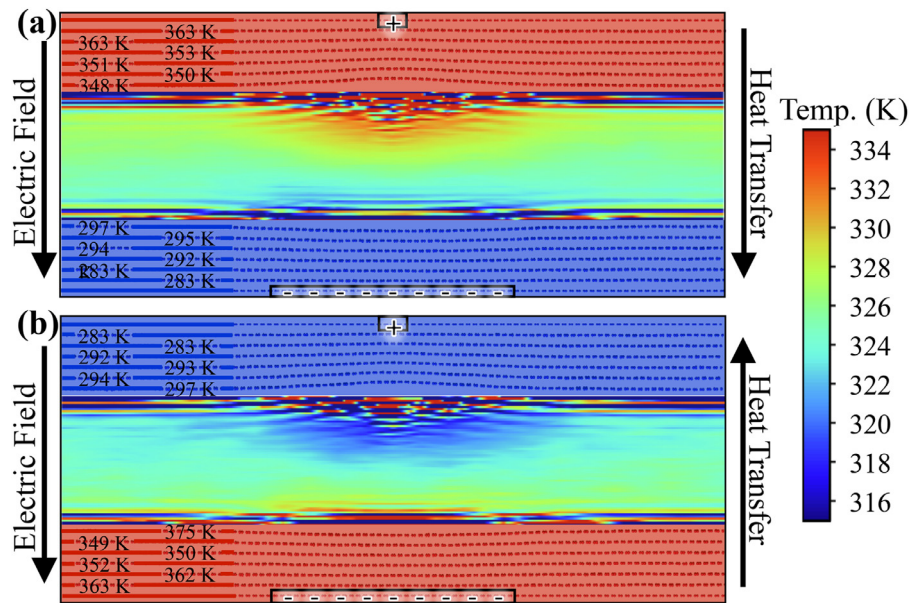
Figure 11. Temperature contours of q_{Plate}=0.075 e case with different heat transfer directions as the pin electrode on **(a)** hot and **(b)** cold reservoir side.

while the periodic regions evidently free from electric field effects. Hence, we can simply state that there is a distinct inhomogeneity in the system. Figure 11 presents the temperature counters of two alignments: the pin electrode is on hot side Figure 11(a)) and pin electrode is on cold side (Figure 11(b)). When the pin electrode was on hot reservoir side, water temperature near the pin electrode was higher than the remaining system due to substantially decreased temperature jump (or increased thermal coupling) between the hot reservoir graphene and water (Figure 11(a)); on the other side of this system, plate electrode creates comparably lower decrease of temperature jump on cold surface, but water near cold plate electrode were at a lower temperature than the rest. An opposite but very similar behavior develops when the heat transfer direction is changed (Figure 11(b)). While the behavior is similar, we focused on the quantitative characterization of heat transfer in these two cases. First, we compared the L_{K-Pin} and $L_{K-Plate}$ values: $L_{K-Pin-Hot}$=2.66 nm and $L_{K-Plate-Cold}$=6.34 nm were measured when the pin is on hot side, and $L_{K-Pin-Cold}$=3.72 nm and $L_{K-Plate-Hot}$=4.59 nm were developed if the pin is on cold side. Through these outcomes, temperature dependent ITR shows itself. Simply, L_{K-Pin} increases when it is on the cold side due to temperature dependence of phonon dynamics, and similarly, $L_{K-Plate}$ decreases when it is on the hot side with enhanced phonon activities. ***The first effect of changing the heat transfer direction is decreasing the difference between*** L_{K-Pin} ***and*** $L_{K-Plate}$. However, increase of L_{K-Pin} and decrease of $L_{K-Plate}$ are almost in the same order that the total ITR in the system remains same. Hence, ITR mechanisms of the current system under a non-uniform electric field does not create any rectification. Second, we focused on the thermal conductivity of the water in these two cases. Even though there is a difference between LDEP forces and resulting water densities and thermal conductivities of opposing pin and plate electrode regions, we observed that this difference is not strong enough to create any rectification. Ultimately, we measured the heat flux in both configuration using Equations (3)-((5) and calculated very similar heat transfer rates on the order of 2 GW/m². As a result, current heat transfer under non-uniform electric field does not show dependence on the direction of heat transfer.

As a final step, we characterized the local variation of heat transfer rates through the system under varying non-uniform electric field. We measured an average heat transfer rate of the

whole system based on Equation (3)-(5) at different electrode charges. Then, we calculated local heat flux values through each region (described in Figure 9) based on their total thermal resistance as $Q_{Local} = (T_{Hot} - T_{Cold})/R_{Local-Total}$. Basically, the total thermal resistance of each local region can be written as $R_{Local-Total} = R_{Gr-H} + R_{K-H} + R_{H_2O} + R_{K-C} + R_{Gr-C}$ where R_{Gr-H} and R_{Gr-C} are the thermal resistances of graphene walls at hot and cold reservoir sides, R_{K-H} and R_{K-C} are the interfacial thermal resistances of the graphene/water interfaces at hot and cold reservoir sides, and R_{H_2O} is the thermal resistance of water in the middle of the two graphene slabs [53]. We calculated the local thermal resistance of water ($R_{H_2O} = L_{H_2O}/k_{H_2O}$) from the thickness of water slab (L_{H_2O}) and its local thermal conductivities (k_{H_2O}). Similarly, we determined graphene thermal resistance ($R_{Gr} = L_{Gr-\parallel}/k_{Gr-\parallel}$) using the local cross-plane thickness ($L_{Gr-\parallel}$) and thermal conductivities of graphene walls in surface normal direction ($k_{Gr-\parallel}$).We should mention here that the high electrode charges ($q_{Plate} \geq 0.75$ e) creating bending of graphene at high electric intensity regions due to LDEP forces result in local increase of cross-plane thermal conductivity of graphene. The thermal resistance of interface is the function of local temperature jump and heat transfer rate as $R_K = \Delta T_{Interface}/q_{Local}$. We would like to underline here that it is important to calculate the interface temperature jump from the temperature fits describing the bulk behavior of both solid and liquid sides. Especially, if any electric charge is applied on just the graphene layer facing the liquid, behavior and the resulting temperature of this graphene layer differentiate from the bulk behavior of few-layer graphene. Calculating a temperature jump between this nearest graphene layer and liquid yields a very erroneous ITR and/or L_K and a misleading characterization of heat transport as done by Ref [10]. Instead, we calculated local temperature jumps from bulk profiles of solid and liquid sides. As the temperature jumps are known, we calculated the local thermal resistance of interface and the heat transfer rate at the corresponding region by a coupled iterative solution. Finally, we obtained local heat transfer rates in each region along the x-direction for every different electrode charges. We validated these local heat flux values by comparing their average with the total heat flux calculation of Equation (3)-(5) and obtained an exact match.

Based on these findings, we determined the heat flux values of pin and plate electrode regions. The local heat transfer rate from
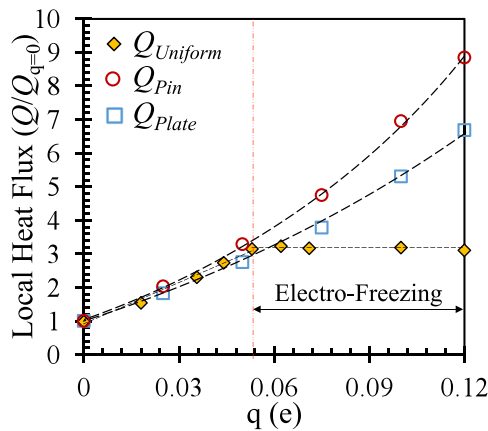
Figure 12. Variation of local heat rates at pin and plate electrode regions under non-uniform electric field as a function of electrode charge. Results of uniform electric field case are given for comparison.

pin electrode region (Q_{Pin}) and the average of local heat fluxes along the plate electrode (Q_{Plate}) are presented in Figure 12. Heat fluxes measured under uniform field ($Q_{Uniform}$) are also given for comparison. Prior to the electro-freezing around q=0.05 e, the $Q_{Uniform}$, Q_{Pin} and Q_{Plate} increases at a very similar rate by increasing the electrode charge. Heat transfer triples for both uniform and non-uniform cases in this charge range. This is expected as the LDEP does not create noteworthy effect at low charge values that heat transfer enhancement of both uniform and non-uniform electric fields remains very similar. As explained previously, the advantage of using a non-uniform electric field for local heat transfer control in low charge range is the difference in size of enhanced heat transfer regions on opposing surfaces allowing to distribute heat from a smaller location to a larger section and/or collect heat to a smaller section from a larger region. Starting with q=0.05 e case, a uniform electric field does not create any further improvements in heat transfer, while heat flux at both pin and plate electrodes of non-uniform field continues to increase substantially by increasing electrode charge, as a result of LDEP. Here, the local heat transfer increase is due to the decrease in total thermal resistance by decreasing temperature jump and increasing water thermal conductivity. At q=0.075 e, a five-times increase of Q_{Pin} develops as a result of decreased L_K with a slightly increased water pressure and resulting thermal conductivity. Starting with q=0.1 e, very low L_K values are obtained that continued increase of heat transfer is mostly due to enhanced thermal conductivity of water in between. At q=0.12 e, a nine-times increase in heat transfer rate is obtained at Q_{Pin}. For such a case, the highly ordered water density reaches to 1.5 gr/cm^3, which is in the range of experimentally observed high pressure water density values [43,49]. The average of heat fluxes over plate electrode region remains lower than the pin electrode results due to comparably lower LDEP forces at large plate electrode regions.

4. Conclusion

Heat transfer between water and few-layer graphene was studied under applied uniform and non-uniform electric fields. Through the electrostatic interactions, both uniform and non-uniform electric fields altered the graphene/water interface energy and created orientation polarization of water by aligning dipoles to the direction of the electric field. In addition to these effects, a non-uniform electric field also created a net force on water molecules towards higher electric field gradient region due to liquid dielectrophoresis (LDEP). We found that these mechanisms can locally manipulate the interfacial thermal resistance, thermal con-

ductivity, and the resulting heat transfer. By increasing the electric field intensity, we measured up to 86% decrease of Kapitza length near electrodes under both uniform and non-uniform electric fields prior to electro-freezing; in this electrode charge range, heat transfer increases up to 3.2 times through electrode regions. With the help of LDEP, non-uniform electric field can create further reduction in interface resistance and yields ultra-low Kapitza resistance values with up to 99% reduction near pin electrode interface. The non-uniform electric field also creates thermal conductivity increase by compressing water such that heat transfer increases up to 9 times at pin electrode region. As a result, we demonstrated that the heat transfer between water and graphene can be controlled actively and locally in two-dimensional space by an applied non-uniform electric field.

Author Statement

O.Y. and M.B. designed the research, O.Y. carried out the computations and analysed the data. O.Y. and M.B. wrote the manuscript togaher.

Declaration of Competing Interest

The authors declare no competing interests.

Acknowledgements

References

[1] Z. Yan, G. Liu, J.M. Khan, A.A. Balandin, Graphene quilts for thermal management of high-power GaN transistors, Nature communications 3 (1) (2012) 1–8.
[2] A.A. Balandin, S. Ghosh, W. Bao, I. Calizo, D. Teweldebrhan, F. Miao, C.N. Lau, Superior thermal conductivity of single-layer graphene, Nano letters 8 (3) (2008) 902–907.
[3] J.B. Wu, M.L. Lin, X. Cong, H.N. Liu, P.H. Tan, Raman spectroscopy of graphene-based materials and its applications in related devices, Chemical Society Reviews 47 (5) (2018) 1822–1873.
[4] J.D. Renteria, D.L. Nika, A.A. Balandin, Graphene thermal properties: applications in thermal management and energy storage, Applied sciences 4 (4) (2014) 525–547.
[5] X. Yu, H. Cheng, M. Zhang, Y. Zhao, L. Qu, G. Shi, Graphene-based smart materials, Nature Reviews Materials 2 (9) (2017) 1–13.
[6] Y. Fu, J. Hansson, Y. Liu, S. Chen, A. Zehri, M.K. Samani, Q. Wang, Graphene related materials for thermal management, 2D Materials 7 (1) (2019) 012001.
[7] C. Qian, B. Ding, Z. Wu, W. Ding, F. Huo, H. He, X. Zhang, Ultralow Thermal Resistance across the Solid–Ionic Liquid Interface Caused by the Charge-Induced Ordered Ionic Layer, Industrial & Engineering Chemistry Research 58 (43) (2019) 20109–20115.
[8] B.Y. Cao, J.H. Zou, G.J. Hu, G.X. Cao, Enhanced thermal transport across multilayer graphene and water by interlayer functionalization, Applied Physics Letters 112 (4) (2018) 041603.
[9] S. Chen, M. Yang, B. Liu, M. Xu, T. Zhang, B. Zhuang, H. Zhang, Enhanced thermal conductance at the graphene–water interface based on functionalized alkane chains, RSC advances 9 (8) (2019) 4563–4570.
[10] Y. Ma, Z. Zhang, J. Chen, K. Sääskilahti, S. Volz, J. Chen, Ordered water layers by interfacial charge decoration leading to an ultra-low Kapitza resistance between graphene and water, Carbon 135 (2018) 263–269.
[11] Z. Ge, D.G. Cahill, P.V. Braun, Thermal conductance of hydrophilic and hydrophobic interfaces, Physical review letters 96 (18) (2006) 186101.
[12] M. Barisik, A. Beskok, Temperature dependence of thermal resistance at the water/silicon interface, International Journal of Thermal Sciences 77 (2014) 47–54.
[13] O. Yenigun, M. Barisik, Effect of nano-film thickness on thermal resistance at water silicon interface, International Journal of Heat and Mass Transfer 134 (2019) 634–640.
[14] A.T. Pham, M. Barisik, B. Kim, Interfacial thermal resistance between the graphene-coated copper and liquid water, International Journal of Heat and Mass Transfer 97 (2016) 422–431.
[15] T.Q. Vo, M. Barisik, B. Kim, Atomic density effects on temperature characteristics and thermal transport at grain boundaries through a proper bin size selection, The Journal of chemical physics 144 (19) (2016) 194707.

[16] A. Pham, M. Barisik, B. Kim, Pressure dependence of Kapitza resistance at gold/water and silicon/water interfaces, The Journal of chemical physics 139 (24) (2013) 244702.

[17] G. McHale, C.V. Brown, M.I. Newton, G.G. Wells, N. Sampara, Dielectrowetting driven spreading of droplets, Physical review letters 107 (18) (2011) 186101.

[18] A.M.J. Edwards, C.V. Brown, M.I. Newton, G. McHale, Dielectrowetting: The past, present and future, Current Opinion in Colloid & Interface Science 36 (2018) 28–36.

[19] W.C. Nelson, C.J.C. Kim, Droplet actuation by electrowetting-on-dielectric (EWOD): A review, Journal of Adhesion Science and Technology 26 (12-17) (2012) 1747–1771.

[20] O. Yenigun, M. Barisik, Electric Field Controlled Heat Transfer Through Silicon and Nano-confined Water, Nanoscale and Microscale Thermophysical Engineering 23 (4) (2019) 304–316.

[21] T.B. Jones, Liquid dielectrophoresis on the microscale, Journal of Electrostatics 51 (2001) 290–299.

[22] X. Zhu, Q. Yuan, Y.P. Zhao, Phase transitions of a water overlayer on charged graphene: from electromelting to electrofreezing, Nanoscale 6 (10) (2014) 5432–5437.

[23] H. Zhao, L. Liu, R. Vellacheri, Y. Lei, Recent advances in designing and fabricating self-supported nanoelectrodes for supercapacitors, Advanced Science 4 (10) (2017) 1700188.

[24] A. Kuzyk, Dielectrophoresis at the nanoscale, Electrophoresis 32 (17) (2011) 2307–2313.

[25] K. Zhao, R. Peng, D. Li, Separation of nanoparticles by a nano-orifice based DC-dielectrophoresis method in a pressure-driven flow, Nanoscale 8 (45) (2016) 18945–18955.

[26] H.J.C. Berendsen, J.R. Grigera, T.P. Straatsma, The missing term in effective pair potentials, Journal of Physical Chemistry 91 (24) (1987) 6269–6271.

[27] T.A. Ho, A. Striolo, Molecular dynamics simulation of the graphene–water interface: comparing water models, Molecular Simulation 40 (14) (2014) 1190–1200.

[28] M. Allen, D. Tildesley, Computer simulation of liquids, Oxford Science, 1990.

[29] Tutein Stuart, Harrison, "A reactive potential for hydrocarbons with intermolecular interactions, J Chem Phys 112 (2000) 6472–6486.

[30] T. Werder, J.H. Walther, R.L. Jaffe, T. Halicioglu, P. Koumoutsakos, On the water− carbon interaction for use in molecular dynamics simulations of graphite and carbon nanotubes, The Journal of Physical Chemistry B 107 (6) (2003) 1345–1352.

[31] H.J. -Richter, C.C. Poon, G. Parker, M. Staffaroni, O. Mosendz, R. Zakai, B.C. Stipe, Direct measurement of the thermal gradient in heat assisted magnetic recording, IEEE Transactions on Magnetics 49 (10) (2013) 5378–5381.

[32] D. Weller, O. Mosendz, H.J. Richter, G. Parker, S. Pisana, T.S. Santos, B. Terris, Sub-nanosecond heat assisted magnetic recording of FePt media, in: Ultrafast Magnetism I, Springer, Cham, 2015, pp. 228–231.

[33] J.H. Irving, J.G. Kirkwood, The statistical mechanical theory of transport processes. IV. The equations of hydrodynamics, The Journal of chemical physics 18 (6) (1950) 817–829.

[34] M.R. Reddy, M. Berkowitz, The dielectric constant of SPC/E water, Chemical physics letters 155 (2) (1989) 173–176.

[35] W.D. Luedtke, J. Gao, U. Landman, Dielectric nanodroplets: Structure, stability, thermodynamics, shape transitions and electrocrystallization in applied electric fields, The Journal of Physical Chemistry C 115 (42) (2011) 20343–20358.

[36] J.Y. Yan, G.N. Patey, Molecular dynamics simulations of ice nucleation by electric fields, The Journal of Physical Chemistry A 116 (26) (2012) 7057–7064.

[37] A.T. Celebi, M. Barisik, A. Beskok, Electric field controlled transport of water in graphene nano-channels, The Journal of Chemical Physics 147 (16) (2017) 164311.

[38] M. Munz, C.E. Giusca, R.L. Myers-Ward, D.K. Gaskill, O. Kazakova, Thickness-dependent hydrophobicity of epitaxial graphene, Acs Nano 9 (8) (2015) 8401–8411.

[39] D. Alexeev, J. Chen, J.H. Walther, K.P. Giapis, P. Angelikopoulos, P. Koumoutsakos, Kapitza resistance between few-layer graphene and water: liquid layering effects, Nano letters 15 (9) (2015) 5744–5749.

[40] H. Han, S. Mérabia, F. Müller-Plathe, Thermal transport at solid–liquid interfaces: High pressure facilitates heat flow through nonlocal liquid structuring, The journal of physical chemistry letters 8 (9) (2017) 1946–1951.

[41] Q.G. Jiang, Z.M. Ao, D.W. Chu, Q. Jiang, Reversible transition of graphene from hydrophobic to hydrophilic in the presence of an electric field, The Journal of Physical Chemistry C 116 (36) (2012) 19321–19326.

[42] J.C. Duda, C.J. Kimmer, W.A. Soffa, X.W. Zhou, R.E. Jones, P.E. Hopkins, Influence of crystallographic orientation and anisotropy on Kapitza conductance via classical molecular dynamics simulations, Journal of Applied Physics 112 (9) (2012) 093515.

[43] B. Chen, W.P. Hsieh, D.G. Cahill, D.R. Trinkle, J. Li, Thermal conductivity of compressed H 2 O to 22 GPa: A test of the Leibfried-Schlömann equation, Physical Review B 83 (13) (2011) 132301.

[44] Y. Mao, Y. Zhang, Thermal conductivity, shear viscosity and specific heat of rigid water models, Chemical Physics Letters 542 (2012) 37–41.

[45] F. Römer, A. Lervik, F. Bresme, Nonequilibrium molecular dynamics simulations of the thermal conductivity of water: A systematic investigation of the SPC/E and TIP4P/2005 models, The Journal of chemical physics 137 (7) (2012) 074503.

[46] John W. Anthony, Richard A. Bideaux, Kenneth W. Bladh, Monte C. Nichols (Eds.), Handbook of Mineralogy. I (Elements, Sulfides, Sulfosalts), US: Mineralogical Society of America, Chantilly, VA, 1990 ISBN 978-0962209703.

[47] A.F. Goncharov, N. Goldman, L.E. Fried, J.C. Crowhurst, I.F.W. Kuo, C.J. Mundy, J.M. Zaug, Dynamic ionization of water under extreme conditions, Physical review letters 94 (12) (2005) 125508.

[48] W. Zhu, Y. Huang, C. Zhu, H.H. Wu, L. Wang, J. Bai, X.C. Zeng, Room temperature electrofreezing of water yields a missing dense ice phase in the phase diagram, Nature communications 10 (1) (2019) 1–7.

[49] I. Iriarte-Carretero, M.A. Gonzalez, F. Bresme, Thermal conductivity of ice polymorphs: a computational study, Physical Chemistry Chemical Physics 20 (16) (2018) 11028–11036.

[50] L. Caretto, D. McDaniel, T. Mincer, N. CSU, Spreadsheet calculations of thermodynamic properties, in: Proceedings of the 2005 American Society for Engineering Education Annual Conference & Exposition, American Society for Engineering Education, Copyright, 2005, June.

[51] A.Y. Nobakht, Y.A. Gandomi, J. Wang, M.H. Bowman, D.C. Marable, B.E. Garrison, S. Shin, Thermal rectification via asymmetric structural defects in graphene, Carbon 132 (2018) 565–572.

[52] N. Wei, S. Li, Y. Zhang, J. Chen, Y. Chen, J. Zhao, Thermal rectification of graphene on substrates with inhomogeneous stiffness, Carbon 154 (2019) 81–89.

[53] M. Barisik, A. Beskok, Boundary treatment effects on molecular dynamics simulations of interface thermal resistance, Journal of Computational Physics 231 (23) (2012) 7881–7892.